

## Physics design of the 8GeV H-minus linac

This content has been downloaded from IOPscience. Please scroll down to see the full text.

2006 New J. Phys. 8 281

(<http://iopscience.iop.org/1367-2630/8/11/281>)

View [the table of contents for this issue](#), or go to the [journal homepage](#) for more

Download details:

IP Address: 139.162.61.215

This content was downloaded on 22/03/2017 at 01:26

Please note that [terms and conditions apply](#).

You may also be interested in:

[Preliminary design and simulation of a 162.5 MHz high-intensity proton RFQ for an accelerator driven system](#)

Xiao Chen, He Yuan, Liu Yong et al.

[Physics design of rod type proton Radio Frequency Quadrupole linac](#)

C. Das, S. Dechoudhury, H.K. Pandey et al.

[IOTA \(Integrable Optics Test Accelerator\): facility and experimental beam physics program](#)

S. Antipov, D. Broemmelsiek, D. Bruhwiler et al.

[Full period superconducting section physics design for injector II of China-ADS](#)

Liu Shu-Hui, Wang Zhi-Jun, Yue Wei-Ming et al.

[Trends in high energy particle accelerators](#)

S Tazzari and M Ferrario

[A particle-in-cell mode beam dynamics simulation of medium energy beam transport for the SSC-Linac](#)

Xiao Chen, He Yuan, Yuan You-Jin et al.

[Longitudinal instability caused by long drifts in the C-ADS injector- I](#)

Li Zhi-Hui, Tang Jing-Yu, Yan Fang et al.

[Conceptional design of a heavy ion linac injector for HIRFL-CSRm](#)

Zhang Xiao-Hu, Yuan You-Jin, Xia Jia-Wen et al.

[Numerical optimization and multi-particle dynamics simulation of the radial matching section of the RFQ](#)

Xiao Chen, He Yuan, Yuan You-Jin et al.

## Physics design of the 8 GeV H-minus linac

**P N Ostroumov**

Argonne National Laboratory, S. Cass Av., Argonne, IL 60439, USA

E-mail: [ostroumov@phy.anl.gov](mailto:ostroumov@phy.anl.gov)

*New Journal of Physics* **8** (2006) 281

Received 22 May 2006

Published 28 November 2006

Online at <http://www.njp.org/>

doi:10.1088/1367-2630/8/11/281

**Abstract.** The proposed 8 GeV proton driver (PD) linac at FNAL is based on 436 independently phased superconducting (SC) resonators (Foster and MacLachlan 2002 *Proc. LINAC-2002* p 826). The linac includes a front end up to  $\sim 420$  MeV and a high energy section operating at 325 and 1300 MHz respectively. A room temperature (RT) radio frequency quadrupole (RFQ) and short H-type resonators are proposed for the initial acceleration of the H-minus or proton beam up to 10 MeV. From 10 to  $\sim 420$  MeV the voltage gain is provided by SC spoke-loaded cavities. In the high-energy section, the acceleration is provided by the International Linear Collider (ILC)-style SC elliptical cell cavities. The beam physics and the lattice design for the FNAL 8 GeV linac are discussed in this paper.

**Contents**

<b>1. Introduction</b>	<b>2</b>
<b>2. Basic parameters</b>	<b>3</b>
2.1. Beam peak current. . . . .	3
2.2. $H^-$ stripping limitations. . . . .	4
<b>3. Choice of major components of the accelerator lattice</b>	<b>5</b>
3.1. Choice of operating frequencies . . . . .	5
3.2. Choice of accelerating structures and transition energies . . . . .	6
3.3. Choice of focusing structure . . . . .	7
3.4. Choice of apertures . . . . .	8
3.5. Block-diagram of the linac . . . . .	8
<b>4. RFQ accelerator</b>	<b>9</b>
4.1. Beam dynamics in the RFQ . . . . .	11
<b>5. MEBT</b>	<b>11</b>
<b>6. Design of the linac lattice downstream of the MEBT</b>	<b>15</b>
<b>7. Beam dynamics simulations</b>	<b>23</b>
7.1. Beam losses . . . . .	24
<b>8. Conclusion</b>	<b>27</b>
<b>Acknowledgments</b>	<b>28</b>
<b>References</b>	<b>28</b>

**1. Introduction**

Recently, Fermilab proposed to develop an 8 GeV  $H^-$  linac, or ‘proton driver’ (PD) [1], with the principal mission to raise the intensity of the Main Injector (MI) to produce so-called super-beams for neutrino studies. In addition, the PD will be capable of producing 2 MW proton beams for fixed target programs including neutrino physics. There are many other possible applications of the PD linac as are discussed in [1, 2]. The original linac proposal was based on three major concepts:

1. Use the SNS linac at a reduced repetition rate of 10 Hz up to 1.2 GeV.
2. Scale the frequency of the TeV-Energy Superconducting (SC) Linear Accelerator (TESLA) resonators and RF system [3] to 1207.5 MHz in order to match to the SNS fundamental frequency of 402.5 MHz and allow for acceleration to the final energy.
3. Adopt the TESLA approach to divide RF power from one large klystron to several cavities [3].

Clearly, implementations of the proposed concepts would significantly reduce the cost of the linac in terms of dollar per voltage ratio compared to the similar ratio for the recently commissioned SNS linac [4].

**Table 1.** Basic parameters of the linac.

Parameter	Value
Particle type for the baseline mission	$H^-$ ions
Beam kinetic energy	8 GeV
Beam current averaged over the pulse	25 mA
Pulse repetition rate	10 Hz
Pulse length	1 ms
Beam pulsed power	200 MW
Beam average power	2 MW
Wall power (estimate)	12.5 MW
Total length	678 m

In this paper, we discuss new design concepts that can further reduce the cost of the 8 GeV linac. Particularly, we propose:

1. Do not scale the frequency of the TESLA or International Linear Collider (ILC) RF system which is 1300 MHz and directly apply SC elliptical cell cavities and klystrons originally developed for the ILC to accelerate  $H^-$  or proton beams above 1.2 GeV.
2. Use squeezed ILC-style (S-ILC) cavities operating at 1300 MHz designed for  $\beta_G = 0.81$  to accelerate protons or  $H^-$  from  $\sim 420$  MeV to 1.2 GeV.
3. To simplify the RF system, it is reasonable and cost-effective to operate the whole linac at no more than two frequencies as is discussed in subsection 3.1. Several options are available for the acceleration of protons up to  $\sim 420$  MeV at 325 MHz which is a sub-harmonic of the ILC frequency.

Application of these concepts to the design of an 8 GeV  $H^-$  linac is discussed in this paper. In the next section, basic parameters of the linac are presented. Major components of the accelerating-focusing lattice are discussed in section 3. The design and beam dynamics simulations in the radio frequency quadrupole (RFQ) and medium energy beam transport (MEBT) are presented in sections 4 and 5 respectively. In section 6, the design procedure for the linac sections above 2.5 MeV are discussed. The results of end-to-end beam dynamics simulations and beam loss studies are presented in section 7. Conclusions are given in the last section.

## 2. Basic parameters

The basic parameters of the 8 GeV  $H^-$  linac are listed in table 1. To reduce the initial cost of the RF system, there is a proposal to operate the linac with reduced beam pulse current at a lower repetition rate as compared to the values listed in table 1. The block-diagram of the proposed linac is given in subsection 3.3.

### 2.1. Beam peak current

The peak beam current plays a significant role in the linac lattice design. The PD is primarily proposed to provide  $N_p = 1.56 \times 10^{14}$  protons per cycle to the FNAL MI. The required peak

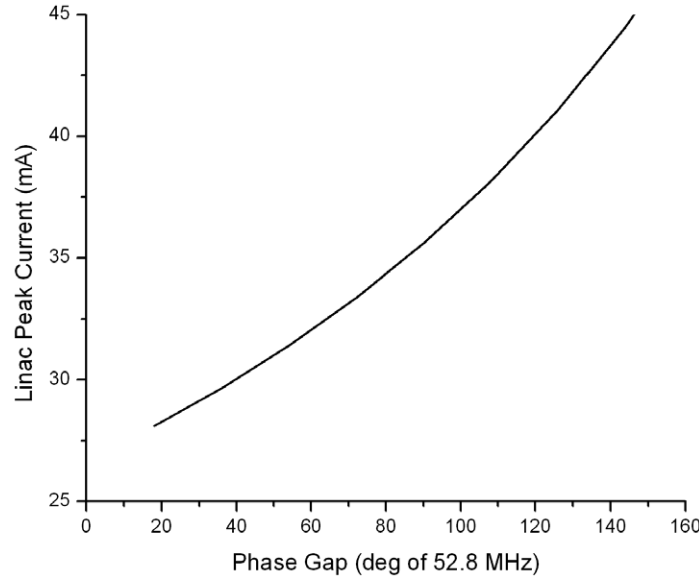


**Figure 1.** Linac beam current as a function of the ‘phase gap’ after injection into the MI.

beam current  $I_p$  is calculated as

$$I_p = \frac{eN_p}{\tau_p} \frac{1}{\eta_k \eta_{rf}},$$

where  $e$  is the elementary charge of the electron,  $\tau_p = 1$  ms is the injection time,  $\eta_k$  is the beam duty factor to provide a gap for the extraction kicker in the MI, and  $\eta_{rf}$  is the beam duty factor to avoid beam losses during the adiabatic bunching of the protons prior to acceleration in the MI. The duty factor  $\eta_k = 0.937$  is defined by the MI revolution period and the  $0.7 \mu\text{s}$  rise-time of the kicker field. It is reasonable to design the linac for the lowest possible peak current to mitigate space charge effects. The latter requires maximizing the duty factor  $\eta_{rf}$ . Figure 1 shows peak beam current as a function of the ‘phase gap’  $\Delta\varphi = 360(1 - \eta_{rf})$  required to avoid beam losses in the MI. The latter depends on the separatrix height in the MI, the energy spread of the 8 GeV beam, and the bunch phase width after the debuncher located upstream of the MI. The current design of the PD has been developed for a 45 mA peak current injected into the RFQ, which results in a peak linac current of 43.25 mA.

## 2.2. $H^-$ stripping limitations

There are several mechanisms resulting in  $H^-$  stripping in accelerators (see, for example, [5]). The main concern is an  $H^-$  stripping in the transverse magnetic field which is transformed to a rest-frame electric field. Following [6], we have calculated the tolerable magnetic field on the pole tip of quadrupoles taking into account the following simplified assumptions:

1. The rest-frame lifetime  $\tau$  of the  $H^-$  is given by the empirical formula [5]:

$$\tau = \frac{3.073 \times 10^{-6}}{E} \exp\left(\frac{44.14 \times 10^9}{E}\right),$$

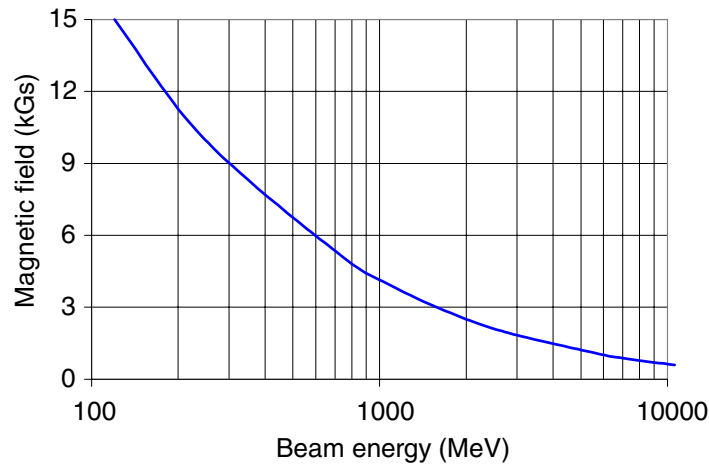


**Figure 2.** Tolerable magnetic field as a function of beam energy.

where  $E = \gamma\beta c B$  is the ion rest-frame transverse electric field,  $\gamma$  is the relativistic parameter,  $\beta c$  is the ion velocity and  $B$  is the transverse magnetic field.

2. The tolerable beam losses are  $0.1 \text{ W m}^{-1}$ .
3. Quadrupoles occupy 10% of the focusing period length.
4. Uniformly distributed beam occupies 70% of the aperture.

These assumptions result to a conservative value of the tolerable magnetic field which is shown in figure 2 as a function of beam energy. Focusing magnetic fields in the linac must be below the curve shown in figure 2.

### 3. Choice of major components of the accelerator lattice

Below we discuss the choice of cavity frequency, linac section transition energies, and the focusing method to be used in the proposed 8 GeV linac.

#### 3.1. Choice of operating frequencies

Eighty five per cent of the total beam energy in the PD linac is provided by the  $\beta_G = 1.0$  ILC cavities. The technology of high-gradient 1300 MHz SC cavities is well established [7] and can be effectively applied for acceleration of high energy protons. As will be seen in section 6, the energy range from 0.4 to 1.2 GeV can be covered by ILC-style reduced beta cavities. The successful development of spoke loaded SC cavities operating at  $\sim 345\text{--}350$  MHz [8] provides a very strong basis for the application of SC structures for energies above in the front end of a multi-GeV linac. The frequency of the front end can be selected to be either the 3rd or 4th sub-harmonic of the 1300 MHz. The 4th sub-harmonic frequency option of the front end as compared to the 3rd sub-harmonic option is preferable for the following reasons:

1. Fewer resonators and associated RF equipment (couplers, phase shifters, circulators) are required to cover the same energy range.

2. Appropriate 324 MHz pulsed power klystrons are available from Toshiba.
3. Spoke loaded cavities are efficient up to  $\sim 400$  MeV where the frequency transition can take place. In a linac, the bunch phase width is a strong function of energy and roughly decreases as  $W^{-3/8}$  [9], where  $W$  is the kinetic energy of the synchronous particle. Having the frequency transition at this high of an energy helps to avoid beam dynamics problems associated with the reduction of the longitudinal stability area [10, 11]. More discussions are presented in section 6.

The FNAL PD will be based on accelerating structures operating at 325 and 1300 MHz. The RF power will be provided by klystrons that have been developed by industry for previous large accelerator projects such as J-PARC in Japan and TESLA, which is the predecessor of the ILC project. The two-frequency option of the FNAL PD has been proposed and discussed in [12].

### 3.2. Choice of accelerating structures and transition energies

As in all recently designed and built hadron linacs, the initial acceleration and focusing will be provided by an RFQ accelerator. For moderate pulse currents of  $\sim 50$  mA, the injection energy into the RFQ can be in the  $\sim 40$ – $90$  keV range. The RFQ injection energy has been selected to be 50 keV and details are given in [13]. The final RFQ energy has been selected to be equal to the SNS RFQ energy which is 2.5 MeV.

Room temperature (RT) drift tube linac (DTL) cavities could provide acceleration up to  $\sim 100$  MeV in the 325 MHz front end of the 8 GeV linac. As is well known, the shunt impedance of drift-tube structures is not high and becomes very low at velocities above  $0.4c$ . As in the SNS or J-PARC linacs, to feed every DTL cavity an individual high-power klystron is required. In the PD linac, it is possible to feed an entire 100 MeV section by a single klystron if SC cavities are used. In order to successfully fan-out RF power from a klystron to multiple cavities, it was proposed to use high-power ferrite vector modulators (FVM) [1]. The latter are required for fast tuning of the cavity complex field and are being successfully developed in several laboratories [3, 14, 15]. Preliminary studies of the proton longitudinal beam dynamics in the linac with multiple cavities powered by a single klystron indicate the feasibility of this approach [16].

SC spoke loaded cavities operating at 352 MHz have been already developed for proton acceleration with an initial energy of 7 MeV [17]. Similar cavities modified to 325 MHz can be used in the PD linac and the transition from RT to SC structures is reasonable to have approximately at 7 MeV or slightly higher as is discussed in section 6. In a SC linac, it is reasonable to minimize number of cavity types to cover the given range of beam velocities for two main reasons:

1. Development of a new type of SC cavity is time-consuming and expensive.
2. The number of lattice transitions in the linac directly corresponds to the number of cavity types and it must be minimized.

To boost beam energy from 2.5 MeV to the value acceptable for the SC cavities, we propose to use RT cross-bar H-type (CH) cavities which have higher shunt impedance than DTL as we have discussed in [18]. The CH cavities have been proposed and are being developed at Frankfurt University as an accelerating structure for high-intensity proton beam injector for future proton synchrotron in GSI [19]. In the PD linac, we propose to use short four- or five-gap CH cavities

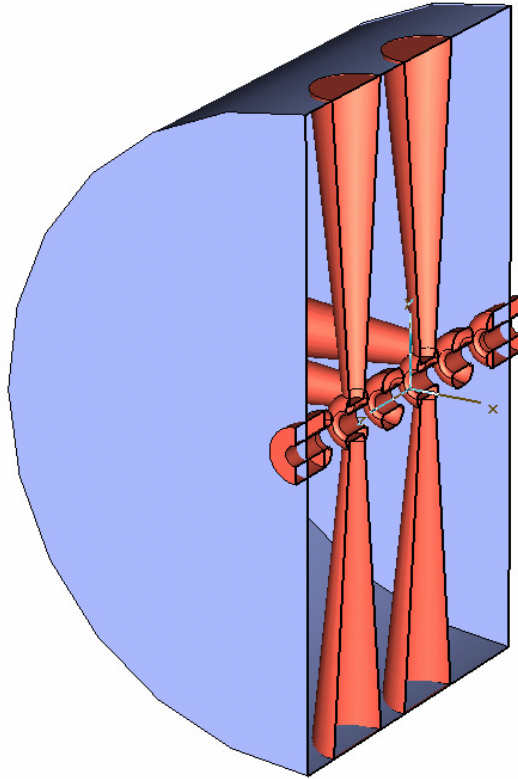


**Figure 3.** Cut-out view of the H-type cross-bar cavity.

alternated by focusing elements. Preliminary model of the cavity is shown in figure 3. Operation on  $\pi$  mode and low capacitive load by small drift tubes result to very high shunt impedance of these cavities which varies from 90 to 60  $\text{M}\Omega \text{ m}^{-1}$  in the energy range from 2.5 to 10 MeV. Further optimization of the CH-cavities is being performed to enhance its shunt impedance and to simplify fabrication technology [20]. Application of CH cavities in the PD linac reduces the power consumption in the initial 10-MeV section by a factor of two as compared to the DTL option.

The SC section of the front end consists of two types of single spoke resonators and triple-spoke resonators (SSR-1, SSR-2 and TSR) and accelerates an  $\text{H}^-$  ion beam up to 420 MeV. The advantages of a single-frequency medium energy proton linac based on multi-spoke cavities have been discussed elsewhere [11].

### 3.3. Choice of focusing structure

In the front end, between the RFQ and TSRs we propose to use SC solenoids for focusing for the following reasons:

1. Axially symmetric beam is less sensitive to space charge effects in the MEBT where the long drift space is necessary to accommodate the chopper and following beam dump.
2. Solenoid focusing can provide a shorter length of the focusing period relative to quadrupole FODO focusing in the RT section of the linac.



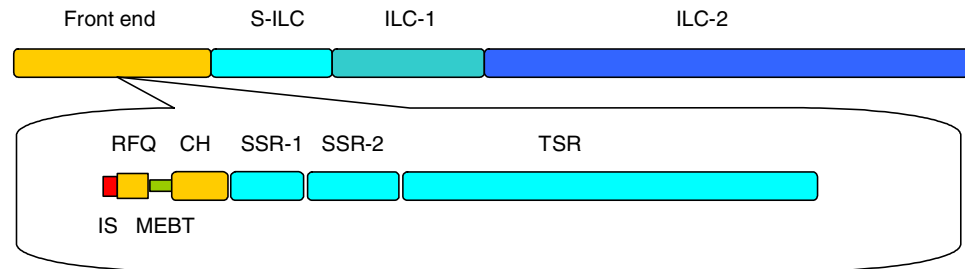


**Figure 4.** Block diagram of the linac.

3. Solenoids can be made with bucking coils and do not require any additional iron shielding in the vicinity of SC resonators. This results in a compact lattice which is very important in the low energy section up to  $\sim 100$  MeV.
4. Above  $\sim 100$  MeV, quadrupole focusing can be used because the beam is less sensitive to the drift spaces between the linac components. In addition, focusing with  $\sim 6$  Tesla solenoids can result in a stripping of the  $H^-$  beam in the fringe fields. The parameters of the proposed linac lattice satisfy the requirements of low beam losses that can take place due to stripping.

Above  $\sim 420$  MeV, the PD design is based on the ILC cryostats FODO structure. This lattice may also be adopted for the SC spoke-loaded resonators in the front end of the linac but up to  $\sim 1$  GeV quadrupole doublets (FDO structure) may be used if they are required by the cryostat design. The FDO structure require longer quadrupoles relative to the FODO structure in the high energy section due to the  $H^-$  stripping limitations.

### 3.4. Choice of apertures

The RFQ aperture is defined from the overall RFQ optimization routine. At the end, the RFQ aperture and vane voltage define the transverse acceptance of the RFQ which is equal to  $2.9 \pi$  mm mrad and much smaller than the acceptance of SC sections of the linac. The apertures of the CH cavities have been chosen to be 18 mm in diameter which is necessary to maximize the shunt impedance of the cavities. At the same time, some beam halo can be intercepted in the RT section of the linac, while the beam energy is lower than  $\sim 10$  MeV. The shunt impedance of SC cavities is a weak function of the aperture. Therefore, the aperture diameter is 30 and 40 mm for the SSRs and TSRs respectively. The ILC cavities have an 70 mm diameter aperture. The aperture budget for the proposed linac has a large margin and makes the probability for beam losses very low.

### 3.5. Block-diagram of the linac

Detailed parameters of the linac and beam dynamics simulation results are presented in the sections 4–7. To clarify the following discussions, we present the block-diagram of the linac in figure 4. The proposed RF distribution system for the linac was presented in figure 2 of [1]. Detailed parameter choices for each linac section will be discussed in section 6 of this paper.

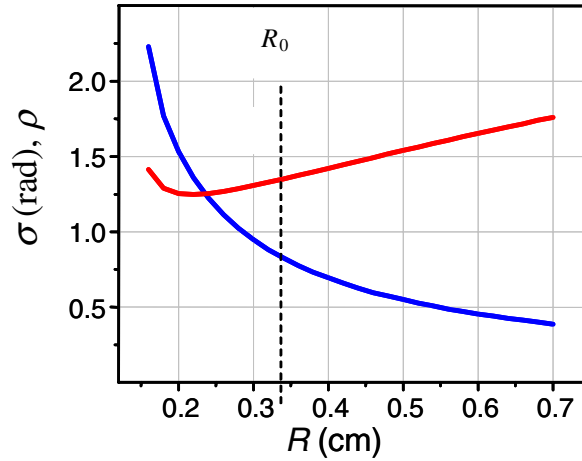


**Figure 5.** The transverse phase advance (the blue curve) and modulus of the Floquet function (the red curve) as a function of the RFQ average radius.

#### 4. RFQ accelerator

The required parameters of the FNAL RFQ are very similar to the SNS [21] and J-PARC [22]. The PD RFQ will operate at 325 MHz and the acceleration of  $\sim 40$  mA pulsed current is considered a relatively moderate problem in the physics design of the RFQ. The design of the RFQ, MEFT and whole PD lattice has been iterated several times to satisfy more advanced RFQ beam specifications. Particularly, the longitudinal emittance must be halo free to avoid excessive beam loss in the high energy section of the PD. Recently, we have reported details of the RFQ design for the PD [13].

For the beam dynamics design, the RFQ is divided into three main sections: an input radial matcher, a main modulated vane section where bunching and acceleration occur, and an output radial matcher. The main section of the RFQ is designed using the code DESRFQ [23]. This code uses a Laplace equation solver, which takes into account the physical vane shape, to generate the RFQ vane tip geometry in every cell and the RFQ parameters required for the final simulations with the TRACK [24] or PARMTEQ [25] codes. The TRACK code tracks particles through the whole RFQ in 3D accounting for both the external and internal space charge fields. The 3D electric field in the regular bunching-accelerating section has been presented by an 8-term Fourier–Bessel expansion.

The first design step is the choice of the average radius  $R_0$ , which can be found using the code DESRFQ. Figure 5 shows the phase advance  $\sigma$  per focusing period and the modulus of the Floquet function  $\rho$  [26] as a function of the average radius calculated for a fixed peak field of  $E_s = 330 \text{ kV cm}^{-1}$  and  $R_e = 0.75R_0$  for unmodulated vanes. Once the average radius is known, the cell-to-cell RFQ parameters and the vane modulation law are generated using the DESRFQ code.

The next step is the multi-particle simulations with the code TRACK. This procedure has been repeated to reach optimum compromise between the following four conflicting requirements: (i) forming low longitudinal emittance, (ii) avoiding transverse rms emittance growth, (iii) maximizing beam transmission, and (iv) maximizing the accelerating rate. Conditions (i) and (ii) can be satisfied at relatively low amplitude of the accelerating field

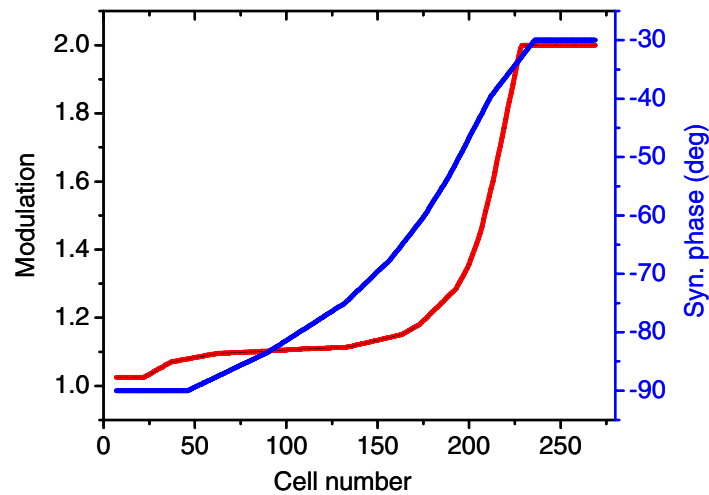


**Figure 6.** Modulation factor (the red curve) and synchronous phase (the blue curve) as a function of cell number.

**Table 2.** Basic RFQ parameters.

Parameter	Value
Input energy (keV)	50
Output energy (MeV)	2.5
Accelerated beam current (mA)	40
Average radius $R_0$ (cm)	0.340
Vane curvature radius $R_e$ (cm)	0.255
Inter-vane voltage $U_0$ (kV)	90.45
Vane length (cm)	302.428
Peak surface field ( $\text{kV cm}^{-1}$ )	330
Normalized transverse acceptance ( $\pi \text{ mm} \cdot \text{mrad}$ )	2.89
Acceleration efficiency <sup>a</sup> (%)	96
Transmission efficiency (%)	97.8
Rms transverse emittance, normalized ( $\pi \text{ mm mrad}$ )	0.25
Longitudinal rms emittance ( $\pi \text{ keV deg}$ )	133
Long. emittance, 99.5% of particles ( $\pi \text{ keV deg}$ )	1886

<sup>a</sup>The acceleration efficiency is defined as a percentage of particles within the energy acceptance of the RFQ (calculated for zero current beam at the RFQ exit) with respect to the injected number of particles.

(small modulation), while the conditions (iii) and (iv) require a higher modulation at initial bunching. The final RFQ vane modulation and synchronous phase as a function of the cell number are given in figure 6. Table 2 presents the final RFQ parameters.

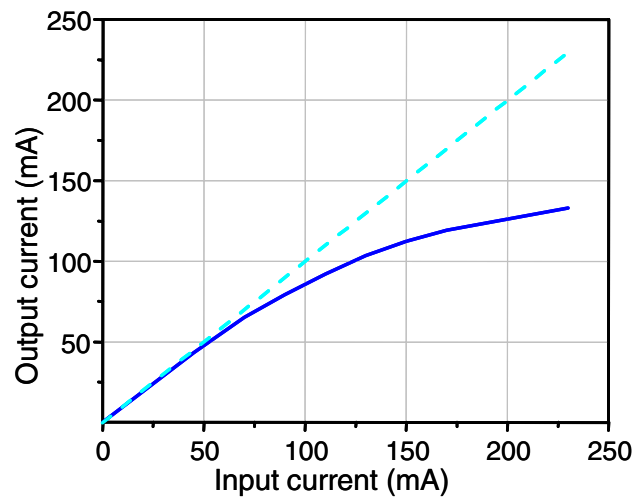


**Figure 7.** Transmission through the RFQ calculated for the same input transverse emittance.

#### 4.1. Beam dynamics in the RFQ

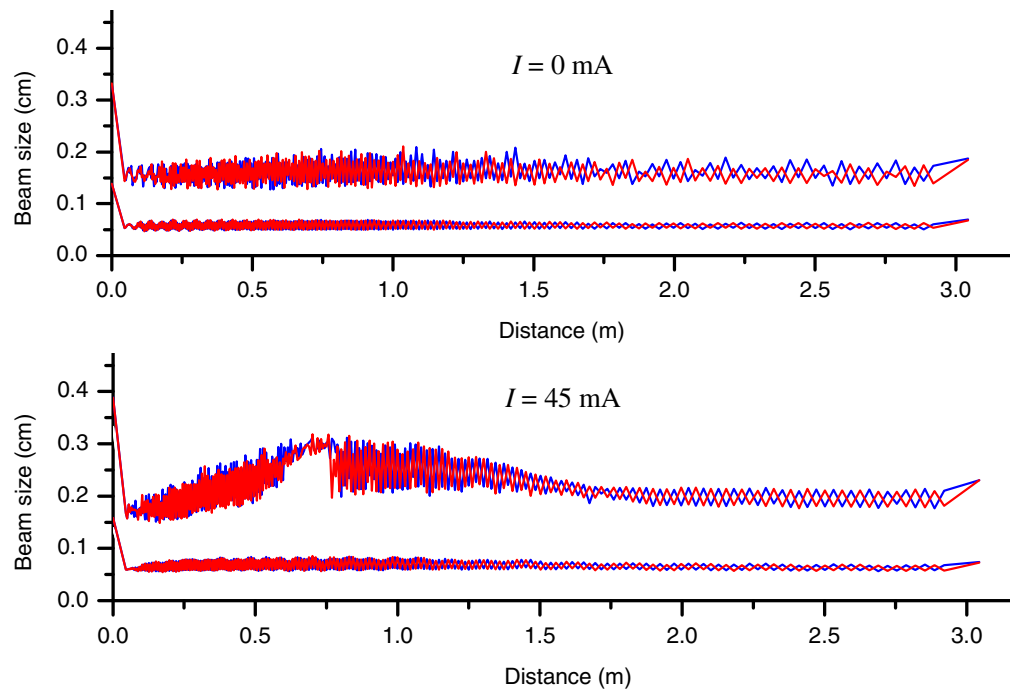
The multi-particle simulations of the RFQ beam dynamics were performed using the TRACK code. Particle motion in a realistic RFQ field is nonlinear and the most comprehensive beam dynamics studies can be carried out by numerical simulations. The proposed design of the RFQ is capable of efficiently accelerating high current beams, which can be seen in figure 7. The current limit of the proposed RFQ can be estimated to be around 140 mA. The simulations have been carried out assuming that the input emittance is a constant independent of the beam current. Beam envelopes calculated by the TRACK code are shown in figure 8. The beam envelope growth along the bunching section reflects some beam halo formation. Further envelope growth is limited by the aperture and particle losses. Despite some halo formation, the total particle losses do not exceed 2% and decreases for lower input beam currents.

After several iterations between DESRFQ and TRACK simulations, the design of the RFQ has been fixed and we performed simulations for a million particles using the TRACK code. The field distribution in the end regions including transition cells was obtained using the electromagnetic studio (EMS) code [27]. The RFQ is provided by the transition cells as was proposed in [28]. In the regular accelerating section the field is calculated using 8-term Fourier-Bessel field expansion. The expansion coefficients have been obtained from DESRFQ.

The emittance and profile of the beam exiting the RFQ are shown in figure 9. The rms and total longitudinal emittances are 134 and  $5309 \pi$  keV deg correspondingly. The total emittance is defined as an ellipse area containing 100% of particles. The ellipse orientation is defined by rms parameters of the particle distribution. The phase space distribution is approximately Gaussian as is seen from figure 10.

## 5. MEBT

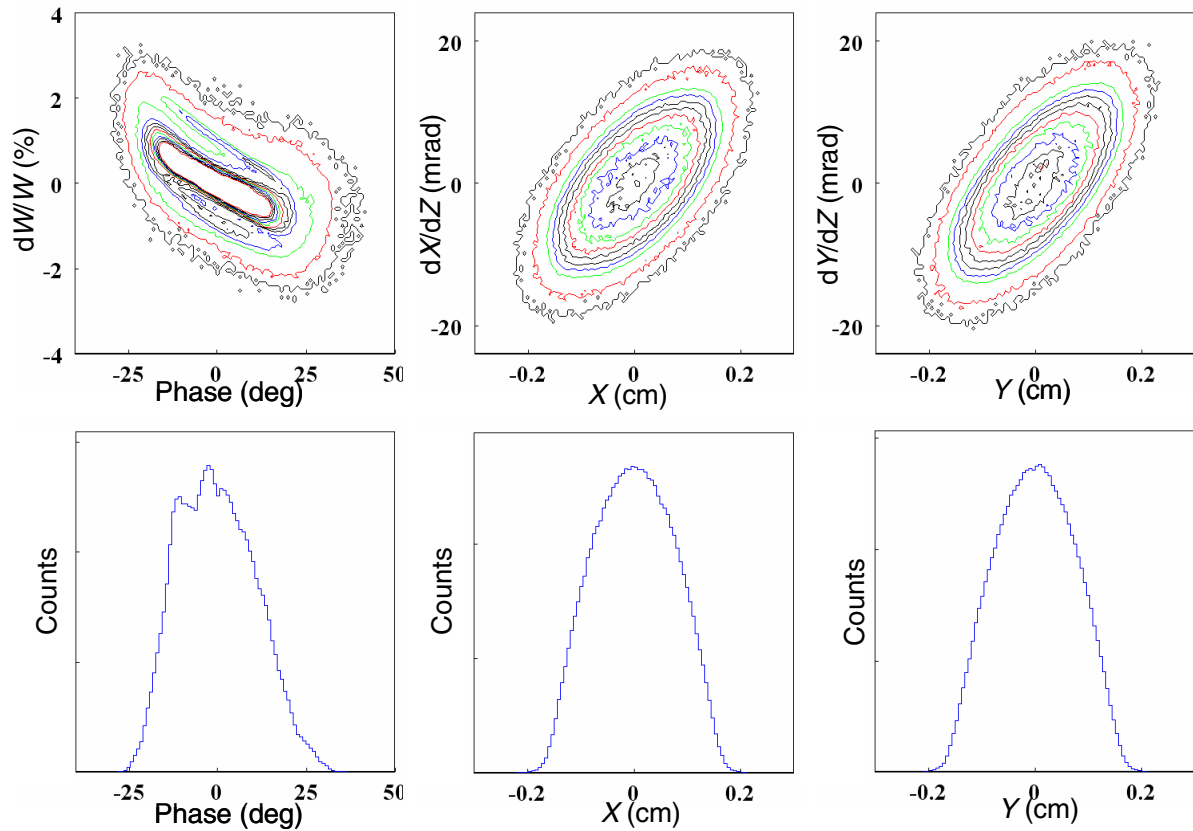
The main function of the MEBT is to provide a space for the fast chopper and matching of the beam into the following linac section. The fast chopper is required to form a gap in the beam



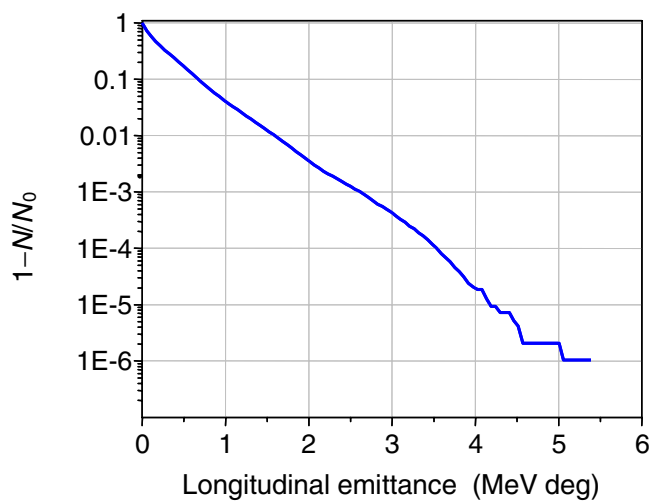
**Figure 8.** Beam envelopes along the RFQ simulated by the TRACK code. The pair of lower curves are beam rms sizes, the upper curves are beam envelopes containing 100% of particles. The blue and red lines correspond to the X- and Y-planes respectively. The beam dimensions extracted at the end of every accelerating cell and radial matchers are connected with the straight lines.

macrostructure for the extraction kicker and to remove one or two out of every six bunches in order to match the beam time structure to 52.8 MHz RF injection frequency of the MI. Four or five bunches will be injected into each separatrix of the MI, during every turn of the multi-turn injection. The 325 MHz bunch frequency is not an integer multiple of the RF frequency of the MI therefore an asynchronism between the bunch frequency and the revolution frequency in the MI helps to avoid building-up high peak current intensities during multi-turn injection into the MI.

The most challenging task is the chopping of the 52.8 MHz time structure with a deflecting voltage rise- and fall-time less than 2 ns. A travelling wave structure (TWS) for this chopper can be similar to those designed at CERN [29] and SNS [30]. We assume that the MI may require an approximately  $120^\circ$  phase gap in the 52.8 MHz time structure which corresponds to 40 mA peak beam current as is seen from figure 1. About 33% of the beam accelerated in the RFQ will be deflected to the beam dump following the chopper. The dumped beam power can be calculated as  $P = E \cdot I_p \cdot (1 - \eta_k \cdot \eta_{rf}) \cdot \eta_b$ , where  $E$  (eV) is the beam kinetic energy, and  $\eta_b$  is the duty factor accounting for the beam pulse repetition rate. For the duty factor  $\eta_b = 0.01$  and 40 mA peak beam current the average power dissipated in the chopper target is  $P = 375$  W. The SNS chopper target [31] has been developed for 400 W average power and a similar target should be suitable for application in the PD. The main chopper parameters are listed in table 3 for the condition where there are no losses on the chopper TWS.



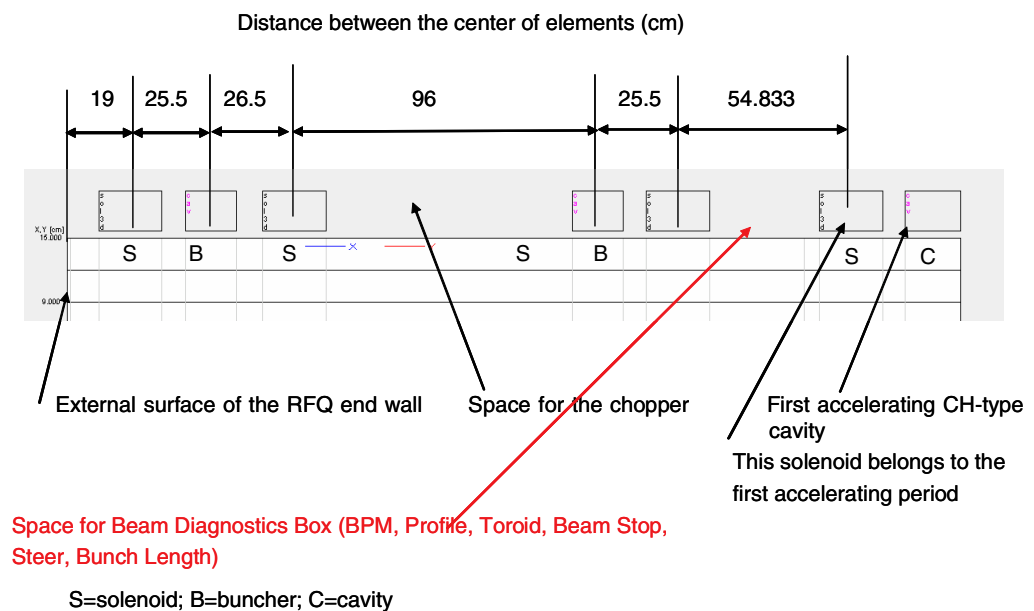
**Figure 9.** Phase space plots (on the top) and beam profiles of the accelerated beam. The outermost isoline contains 100% of particles; the next isoline contains 99% of particles.



**Figure 10.** Fraction of particles outside of the given emittance as a function of the longitudinal emittance.  $N$  is the number of particles within the given longitudinal emittance (horizontal axis), while  $N_0$  is the total number of particles.

**Table 3.** Basic parameters of the chopper.

Parameter	Value
Length of the TWS	50 cm
Required voltage at 100% efficiency of the TWS	$\pm 1.92$ kV
Distance between the deflecting plates	16 mm
Rise- and fall-time of the voltage pulse	2 ns
Repetition frequency	52.8 MHz
Duty cycle	1%
Average beam power on the beam dump	375 W
Pulsed beam power on the beam dump	37.5 kW

**Figure 11.** The MEBT structure.

The MEBT provides an  $\sim 75$  cm drift space to accommodate the TWS following the beam collimator. Such a long drift space is possible using SC solenoids for the beam focusing in the MEBT. To provide the longitudinal matching two rebunchers are required as is shown in figure 11. In addition, the first CH cavity should operate in the rebuncher mode for high current beams. The length for the chopper space is restricted mainly by the longitudinal beam dynamics as is discussed in subsection 7.1. Shortening of the drift space for the chopper improves beam parameters over the whole accelerator, therefore it is very important to develop a voltage pulser with superior parameters compared to those given in table 3. Figure 12 shows the transverse envelopes of the deflected bunches.

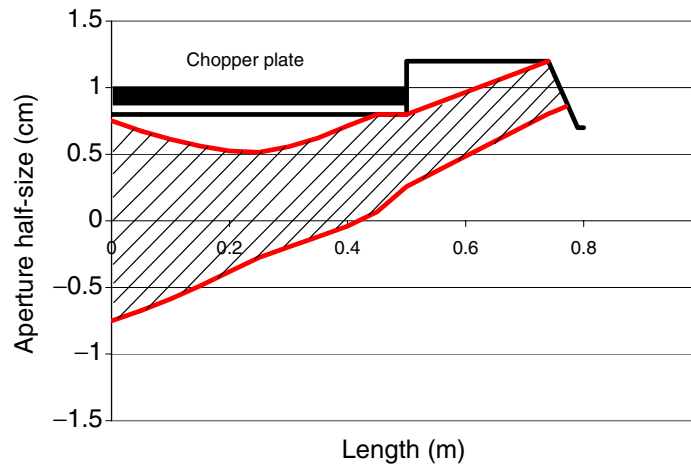


**Figure 12.** Envelope of the deflected bunches. The longitudinal coordinate origin coincides with the beginning of the TWS. The bold black line is the aperture of the TWS and collimators.

## 6. Design of the linac lattice downstream of the MEBT

Earlier studies carried out at LANL (see, for example, [32]) have established the requirements for the lattice of high-intensity proton linacs necessary to avoid beam rms emittance growth along the linac:

1. Phase advance per focusing period of transverse oscillations for zero current beams should be below  $90^\circ$ .
2. Wavenumbers of both transverse and longitudinal oscillations  $k_{x0}$ ,  $k_{y0}$  and  $k_{z0}$  must change adiabatically along the linac. This requirement should be also applied to the lattice transitions with different types of focusing. Adiabatic change of real-estate accelerating gradients and focusing fields are required to fulfil these conditions.
3. Avoid strong space charge resonances. The space charge resonances are convenient to analyse using I. Hofmann's chart [33].
4. Provide equipartitioning of betatron and synchrotron oscillation temperatures along the linac [26].
5. Beam matching in the lattice transitions is very important to avoid appreciable beam halo formation.

In the linacs with space-charge dominated beams, all these conditions must be satisfied. The condition of space charge dominated beams is defined in [26]

$$\frac{\sigma}{\sigma_0} \leq \frac{1}{\sqrt{2}}, \quad (1)$$

where  $\sigma_0$  and  $\sigma$  are the phase advances of particle oscillations in the beam without and with space charge calculated over a focusing period. In normal conducting linacs designed for acceleration of beams with peak current up to  $\sim 150$  mA, all the above-listed requirements can be fulfilled as was shown in several publications (see, for example, [34, 35]). SC linacs also can be designed



to satisfy high-current specifications [35]. However, such a design will be expensive due to the increased number of cavities and cryostats. A cost-effective design of SC linac will have the following properties:

1. The acceleration is provided with several types of cavities designed for fixed beam velocity. For the same SC cavity voltage performance, there is a significant variation of real-estate accelerating gradient as a function of the beam velocity.
2. The length of the focusing period for a given type of cavity is fixed.
3. There is a sharp change in the focusing period length in the transitions between the linac sections with different types of cavities.
4. The cavities and focusing elements are combined into relatively long cryostats with an inevitable drift space between them. There are several focusing periods within a cryostat.

In the following sections of this paper, we will discuss how to mitigate the effects of lattice transitions in a SC linac and achieve high beam quality for moderate peak beam currents of  $\sim 40$  mA as is required for the PD. By applying strong focusing, both in the transverse and longitudinal planes condition (1) can be avoided in the PD linac design. Exact fulfilment of the equipartitioning condition in the PD linac will result in a reduced energy gain and longer linac. Following the recommendation of [26], we minimize the deviation of the beam parameters from the equipartitioning condition which helps to avoid excess emittance growth.

There is another important parameter in SC linacs that should be taken into account in the lattice design. Due to the high accelerating gradients of SC cavities and the relatively long focusing periods, a parametric resonance of transverse oscillations can easily take place [36]. The resonance is strong and must be avoided by appropriate lattice design.

The lattice design of a SC linac includes the following main steps:

1. Select the geometric beta of the cavities using a simplified formula for the cavity Transit Time Factor (TTF).
2. Select the type of cavities that are suitable for the given velocity range. Optimize the electrodynamics and the mechanical design of the cavities. By numerical simulation, design the cavities to reduce the ratio of peak surface fields to the accelerating field.
3. Assume experimentally proven peak surface fields in SC cavities. Use the ratio of the peak surface field to the accelerating field obtained from optimized cavity geometry.
4. Select the focusing lattice taking into account the above mentioned requirements. Select the cryostat length and inter-cryostat spaces working with cryogenic and mechanical engineers.
5. Develop lattice tuning for the beam without space charge. Avoid zero-current resonances. Usually two types of strong parametric resonances may cause problem: parametric resonance of transverse motion [9, 36] and parametric resonance of longitudinal motion (or ‘structure resonance’), as was discussed, for example, in [37, 38].
6. Using rms envelope equations check the lattice tune to verify and avoid strong space charge resonances.
7. Provide matching of the beam for the design peak current in all lattice transitions.
8. Simulate beam dynamics using multi-particle codes. Study beam losses using a large number of multi-particles,  $\sim 10^6$ .

**Table 4.** Focusing lattice. S solenoid; R resonator; F D quadrupoles,  $L_p$  length of the focusing period;  $L_E$  effective length of the focusing element.

Section	CH	SSR-1	SSR-2	TSR	S-ILC	ILC-1	ILC-2
Focusing	SR	SR	SRR	FRDR	FR <sup>2</sup> DR <sup>2a</sup>	FR <sup>4</sup> DR <sup>3</sup>	FR <sup>8</sup> DR <sup>8</sup>
Length of the focusing period $L_p$ (m)	0.515–0.75	0.75	1.60	3.81	6.1	12.2	24.4
Aperture radius (cm)	1.0	1.5	1.5	2.0	3.05	3.5	3.5
$B^b$ (T)	$\leq 5.8$	$\leq 5.6$	$\leq 6.2$	$\leq 0.24$	$\leq 0.15$	$\leq 0.1$	$\leq 0.081$
Effective length $L_E^c$ (cm)	11.238	8.192	18.559	20.0	40.0	50.0	50.0

<sup>a</sup> $R^2 = RR$ .<sup>b</sup>Magnetic field of quadrupoles is given on the pole tip for which the radial position is equal to the aperture radius. Magnetic field of solenoids is given at the centre of solenoids.<sup>c</sup>The effective length is calculated at the 6 T field level in the centre of solenoid.**Table 5.** Cavity parameters.

Section	CH	SSR-1	SSR-2	TSR	S-ILC	ILC-1	ILC-2
$\beta_G$	–	0.2	0.4	0.6	0.83	1.0	1.0
Number of resonators	16	18	33	42	56	63	224
Number of cells	4–5	2	2	4	8	9	9
Number of cryostats	–	2	3	7	7	9	28
Peak surface field (MV m <sup>-1</sup> )	–	30	28	30	52	52	52
Accelerating voltage (MV)	0.25–1.0	1.5	3.25	9.31	17.72	27	27
Accelerating gradient (MV m <sup>-1</sup> )	1.8–3.0	11.5	8.64	9.65	23.7	26	26
Cryostat length (m)	–	6.85	9.4	10.9	12.2	12.2	12.2

Iterate this procedure to obtain a linac design which satisfies the engineering requirements and provides high quality accelerated beams.

We have applied this procedure for the lattice design of the FNAL PD. Tables 4 and 5 show the final basic parameters of the focusing and accelerating elements. The first step of the above mentioned iterative procedure defines preliminary number, type of SC cavities and transition energies. For this analysis, we have derived the following formulae for the TTF of cavities operating on  $\pi$ -mode of electromagnetic oscillations which is the case for practically all known types of SC cavities:

$$T_C(N, \beta, \beta_G) = \begin{cases} \left(\frac{\beta}{\beta_G}\right)^2 \cos\left(\frac{\pi N}{2\beta/\beta_G}\right) \frac{(-1)^{(N-1)/2}}{N((\beta/\beta_G)^2 - 1)}, & \text{if } \beta \neq \beta_G, \\ \frac{\pi}{4}, & \text{if } \beta = \beta_G, \end{cases}$$

for an odd number of cells  $N$  in the cavity and

$$T_S(N, \beta, \beta_G) = \begin{cases} \left(\frac{\beta}{\beta_G}\right)^2 \sin\left(\frac{\pi N}{2\beta/\beta_G}\right) \frac{(-1)^{(N+2)/2}}{N((\beta/\beta_G)^2 - 1)}, & \text{if } \beta \neq \beta_G \\ \frac{\pi}{4}, & \text{if } \beta = \beta_G, \end{cases}$$

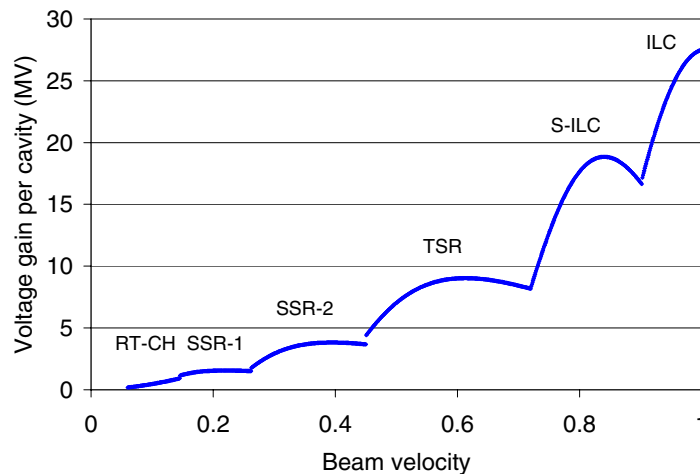


**Figure 13.** Voltage gain per cavity as a function of beam velocity.

for an even number of cells  $N$  in the cavity. Using cavity parameters similar to those given in table 5, the energy gain in the linac composed of several types of cavities can be calculated. The goal of this exercise is to minimize the total number of cavities. Transition energies have been selected to equalize the voltage gain in the transition region. Typical voltage gain in the 8 GeV linac is shown in figure 13. The geometrical betas of spoke-loaded SC cavities are selected to cover a velocity range from  $0.145c$  to  $0.724c$  with the lowest number of cavities. In this velocity range, it is not reasonable to reduce the number of cavity types to two due to an appreciable increase in the number of cavities which is caused by the large variation of the cavity's TTF.

Once the ILC cavities exist, the S-ILC cavity type must have  $\beta_G = 0.81$  to minimize the number of cavities to match beam velocity to ILC cavities. Final values of transition energies depend on the cryostat design and beam dynamics requirements as is discussed above.

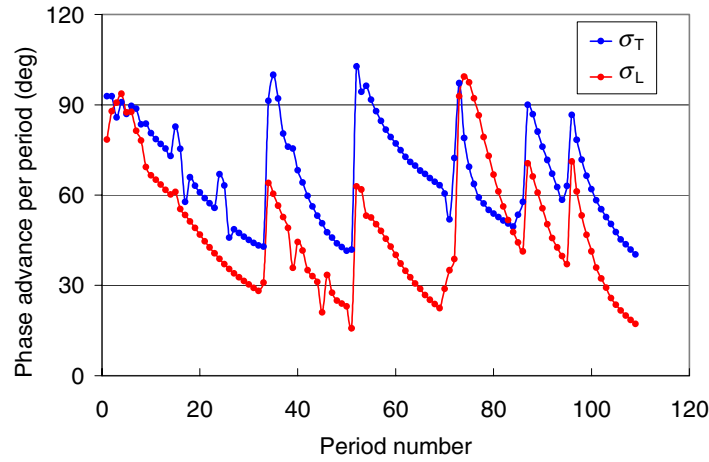
The most expensive part of the linac is the high-energy section where the ILC cryostats can be used for the acceleration. This section of the linac has been designed to use the exact same ILC cryostats that have been developed for the future electron-positron collider. However, in the energy range 1.2 to 2.4 GeV, the focusing period provided by the ILC cryostats is too long and the conditions for parametric resonance occur. Therefore, in our design we use the same ILC cryostat but replace one SC cavity with a focusing quadrupole, resulting in the focusing period length being reduced by a factor of two.

We have analysed the transition energy between the RT and SC structures and found that 10 MeV is the optimal transition energy. At 10 MeV, the energy gains per cavity both in the RT and the SC sections are equal, and the beam energy is high enough to allow a short drift space to provide for the warm-cold transition. In addition, the proposed CH cavities have very high shunt impedance below 10 MeV.

In the energy range from 30 to 120 MeV, both double-spoke and single spoke cavities are effective. To provide for an adiabatic change of the focusing parameters, the focusing period length should be within 1.5–2.0 m. Therefore the lattice containing two SSRs designed for  $\beta_G = 0.4$  and a solenoid is a good choice. The geometrical beta of the SSR-2 cavities has been included into the iteration procedure of the lattice design. The best beam quality was obtained with the design parameters given in tables 4 and 5. Table 6 shows transition energies and coordinates of the section ends in the final design.

**Table 6.** Beam energies and coordinates of the section ends along the linac.

Section	RFQ	MEBT	CH	SSR-1	SSR-2	TSR	S-ILC	ILC-1	ILC-2
Beam energy (MeV)	2.5	2.5	10	32	124	421	1223	2445	8000
Coordinate (m)	4.0	6.65	17.0	31.4	61.0	142.2	226.7	336.5	678.1

**Figure 14.** Transverse and longitudinal phase advances along the linac

The following figures 14–20 show the final lattice parameters of the PD. Figure 14 shows the variation of the phase advance of transverse and longitudinal oscillations per focusing period along the linac calculated for a zero-current beam. The phase advances are calculated numerically using the matrix calculation routine incorporated into the TRACK code. A probe particle is traced through the focusing period with realistic fields and calculates the first order transport matrix. Jumps in the phase advances from  $\sim 45^\circ$  to  $\sim 90^\circ$  are related to the transitions between different types of SC cavities. The stability diagram for the transverse motion calculated for the zero-current beam is shown in figure 15. Following I M Kapchinskiy [9], we present the stability diagram using  $\cos(\sigma_T)$  as a function of the defocusing factor

$$\Delta_s = \frac{\pi}{2} \frac{1}{(\beta\gamma)^3} \frac{S_f^2}{\lambda} \frac{eE_m \sin \varphi_s}{m_0 c^2},$$

where  $m_0$  is the particle rest mass,  $c$  is the speed of light,  $\beta$  is the particle relative velocity,  $\gamma$  is the relativistic factor,  $\lambda$  is the wavelength of the RF field,  $S_f$  is the length of the focusing period and  $E_m$  is the amplitude of the equivalent travelling wave of the accelerating field,  $\varphi_s$  is the synchronous phase. In the diagram, the upper blue line corresponds to the boundary of parametric resonance of the betatron motion, while the dashed line corresponds to the stability required for the particles near the separatrix boundary at a phase angle of  $-2|\varphi_s|$ . The linac comprises 110 focusing periods downstream of the MEBT and the majority of the tune points are located inside the stability region. However, for beam matching purposes in the lattice transitions, we need to adjust the fields in the focusing elements. These tune points are located outside the stability region, but because the instability takes place over a short distance compared to the betatron oscillation wavelength, the unstable tune points do not affect the beam quality.

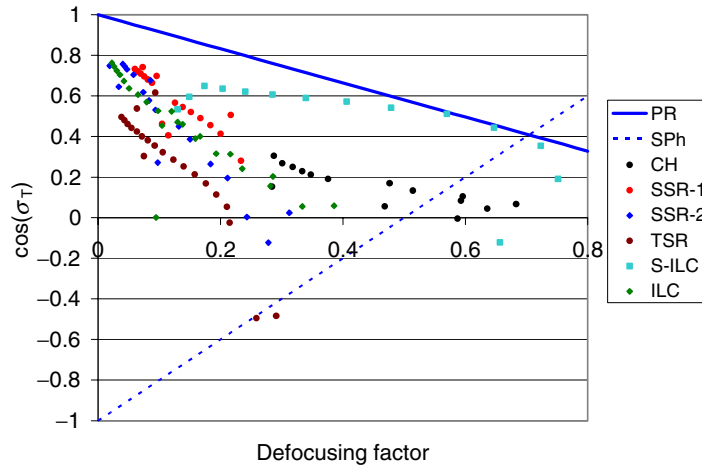


**Figure 15.** Stability diagram for the beam with zero current shown as a function of  $\cos(\sigma_T)$  versus the defocusing factor. The dots represent tunes in each period of the different lattice sections. The solid blue line shows the boundary of the parametric resonance of the betatron oscillations, the dashed blue line corresponds to the transverse stability of particles located near the separatrix of the longitudinal oscillations.

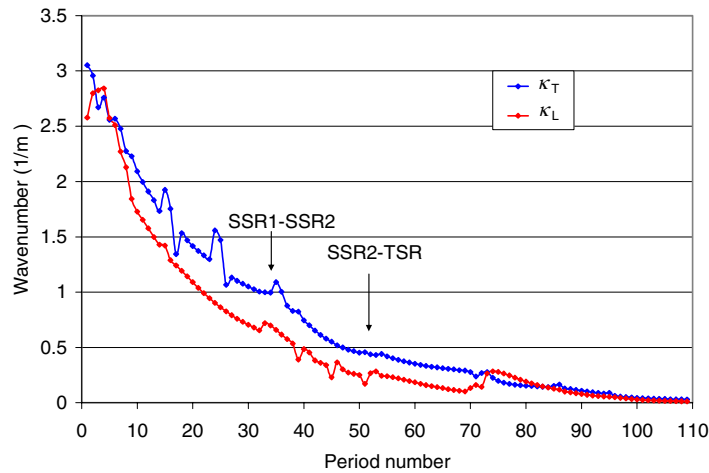


**Figure 16.** Wavenumbers of transverse and longitudinal oscillations along the linac.

Figure 16 shows evolution of wavenumbers of transverse and longitudinal oscillations along the linac calculated for a zero-current beam. In a high-current linac (above  $\sim 100$  mA), this type of curve should be smooth without any jumps. In figure 16, notice the irregular jumps of the wavenumbers which are necessary for beam matching in the inter-cryostat spaces and in the lattice transitions. The simulations show that any beam mismatch in the lattice transitions results in rapid emittance growth.

The wavenumbers of particle oscillations can be expressed as:

$$k_{x0} = \frac{\sigma_{x0}}{L_f}, \quad k_{y0} = \frac{\sigma_{y0}}{L_f}, \quad k_{z0} = \frac{\sigma_{z0}}{L_f}.$$

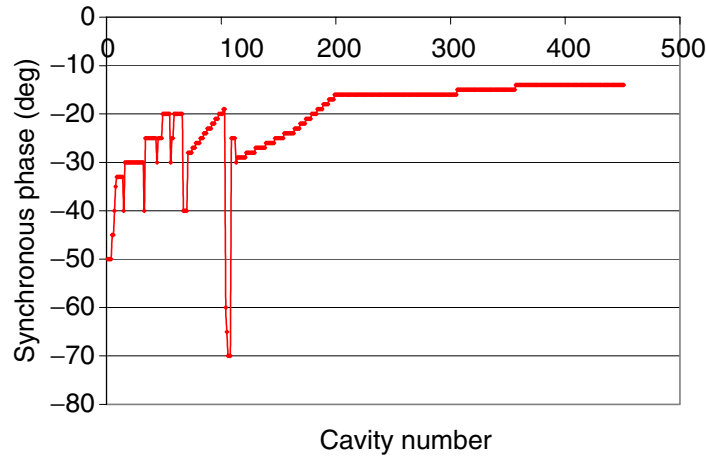


**Figure 17.** Cavity phase as a function of the cavity number.

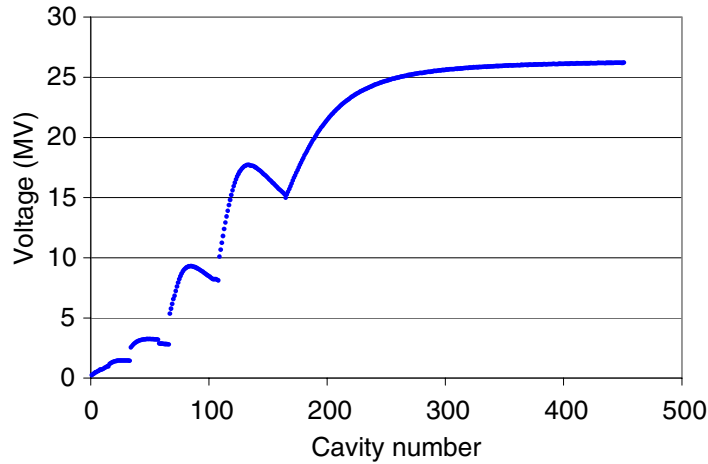


**Figure 18.** Voltage gain per cavity.

The linac lattice has been tuned to provide the same wavenumbers for both horizontal and vertical oscillations, therefore we use the notation  $\sigma_{T0} = \sigma_{x0} = \sigma_{y0}$ ,  $\sigma_{L0} = \sigma_{z0}$ ,  $k_{T0} = k_{x0} = k_{y0}$ ,  $k_{L0} = k_{z0}$ . The smooth change of the betatron oscillation wavenumber is provided by selecting the appropriate length of the focusing periods as is shown in table 4 and the focusing field strength. The smooth change of the wavenumber of longitudinal oscillations is provided mainly by adjusting the synchronous phase. As a synchronous phase, we assume the phase angle of the RF field in the cavity with respect to the cavity field phase that provides maximum energy gain for given particle velocity. Figures 17 and 18 show the phase setting in the cavities and voltage gain per cavity respectively.

Adiabatic change of the wave-numbers for the betatron and synchrotron oscillations ( $k_{T0}, k_{L0}$ ) along the linac provide a ‘current independent’ tune of the linac lattice and such a concept has been applied for the design of several high-intensity linacs including the SNS [39] and proposed SPL at CERN [40]. To mitigate higher order resonances due to space charge related coupling between the phase space planes, the tune depression due to the space charge should be low. For this reason, the transverse phase advances in the PD lattice tune have been selected to be

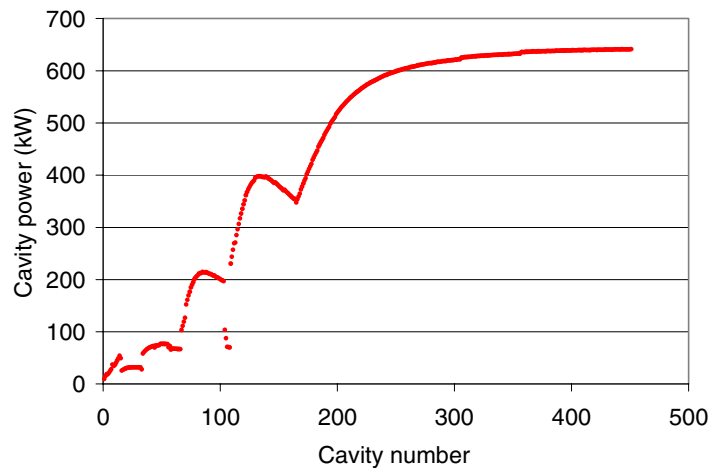


**Figure 19.** Total power per cavity as a function of the cavity number.

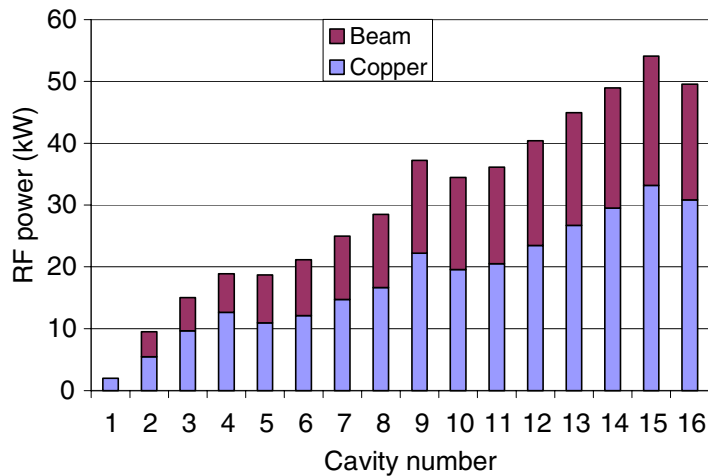


**Figure 20.** Total power per cavity as a function of the cavity number for the RT CH cavities.

above  $45^\circ$ , figure 14. Final tunes have been chosen using Hofmann's chart [33]. Although exact equipartitioning of oscillations is not required, the beam remains close to the equipartitioning condition throughout most of the linac below 1 GeV.

The linac has a four-fold frequency transition which complicates the adiabatic matching of the synchrotron motion. In principle, such a matching can be provided by a long adiabatic section which would be an expensive piece of the linac. In this design of the PD, the matching is provided by a  $90^\circ$  'bunch rotation' in the longitudinal phase space which requires  $-60^\circ$  and  $-70^\circ$  phase setting in the last five TSRs, figure 17. Correspondingly, there is a jump in the wave number of synchrotron oscillations in period number 73 as is seen in figure 16. This matching technique may require retuning of the phases of the cavities located near the transition region for appropriate matching of beams at different currents. However, as will be seen in the following section, the transition is relevant across the full range of beam currents from 0 to  $\sim 40$  mA.

Figure 19 shows the required RF power to compensate beam loading and cavity wall losses (in the CH cavities) as a function of the cavity number. In the SC cavities, the power dissipated

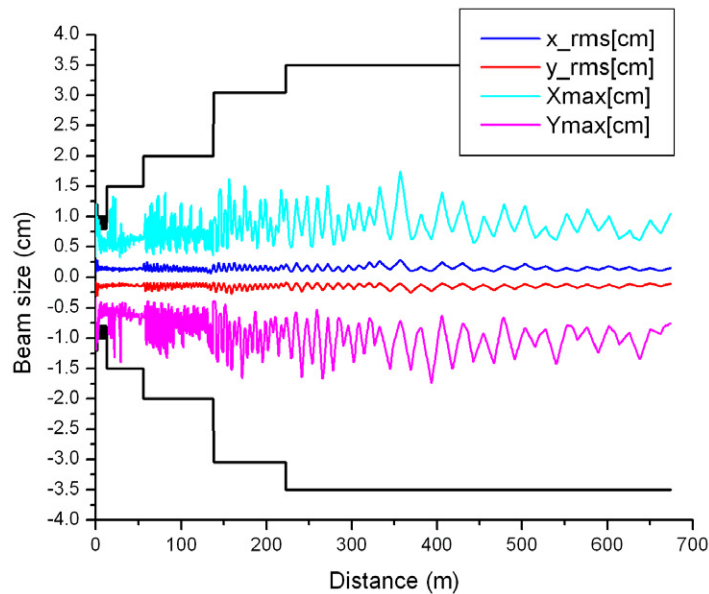


**Figure 21.** Transverse envelopes of 43.25 mA beam along the linac. The black solid line shows the aperture.

in the cavity walls is negligible, while in the RT cavities the dissipated power is comparable with the beam power as is seen from figure 20. This data is necessary for the design of the power fan-out system.

## 7. Beam dynamics simulations

Prior to the beam dynamics simulations, a careful matching of the 43.25 mA beam Twiss parameters in the lattice and inter-cryostat transitions was made using the codes TRACE3D [41] and TRACK [24]. The code TRACK tracks particles in realistic 3D fields in all accelerator elements and the TRACE3D results have been iterated to obtain acceptable beam matching. The simulation starts with a 45 mA  $H^-$  dc beam at the entrance of the RFQ with an initial water-bag distribution represented by one million particles. About 4% of the beam injected into the RFQ is not accelerated and is intercepted by the RFQ vanes and MEBT collimators. Figures 21 and 22 show rms and total envelopes of the beam along the linac. The total and rms phase width along the linac are shown in figure 23. Figures 24 and 25 show the emittance growth in all three phase planes along the linac, which is at an acceptable level of and caused mainly by imperfections of beam matching in the lattice transitions. Finally, the phase space plots at the end of the linac are shown in figure 26, where some halo development in all phase planes can be observed.

End-to-end beam dynamics simulations have been performed for the same lattice tune as for the 45 mA beam with a different input current of 32.5 mA. Only four quadrupoles in the transition from solenoid focusing to FODO have been slightly retuned for better beam matching. The results of these simulations are shown in figures 27 and 28. As expected, the growth of rms emittance is noticeably lower than for the higher current beam. We do not present here the simulation results for lower currents. We have found that the emittance growth and the envelopes of lower currents beam for the same lattice tune are smaller than the 43.25 mA beam results.



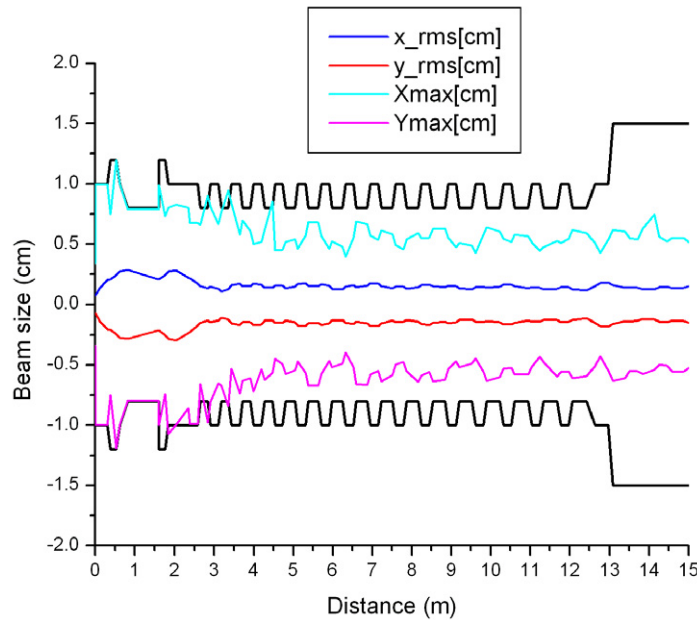


**Figure 22.** Transverse envelopes of 43.25 mA beam along the MEBT and CH section of the linac. The black solid line shows the aperture.

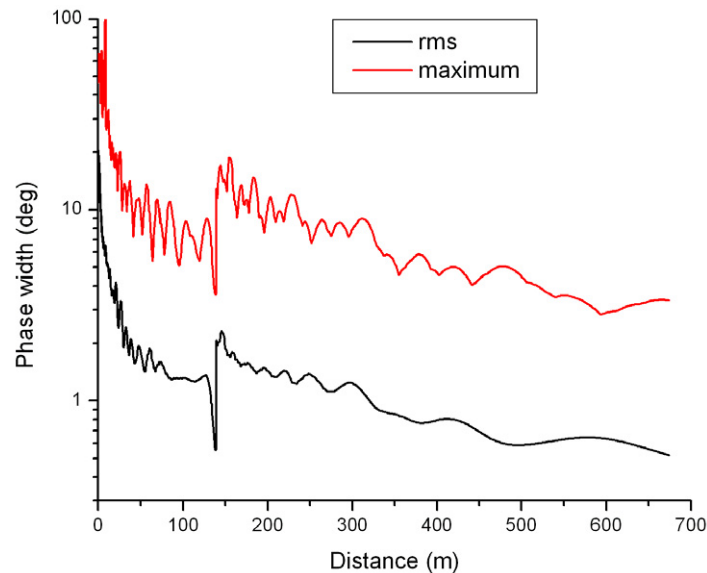


**Figure 23.** RMS and maximum phase half-width envelopes along the linac.

### 7.1. Beam losses

Some fraction of the beam lying outside of the RFQ transverse acceptance will be lost at the RFQ entrance. In the RFQ and downstream, the energy of the majority of the lost particles is in the range  $\sim 30$ – $100$  keV. At the peak design current of 45 mA, the RFQ accelerates 96% of the particles within the transverse acceptance. 2.2% of the particles will be lost inside the RFQ. 1.8% of particles are transmitted through the RFQ and are intercepted by the collimators in the

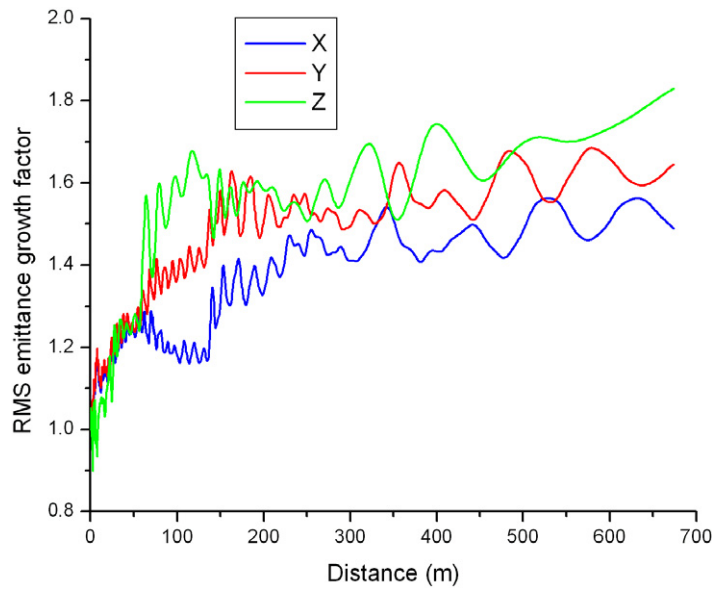


**Figure 24.** RMS emittance growth factor along the linac.

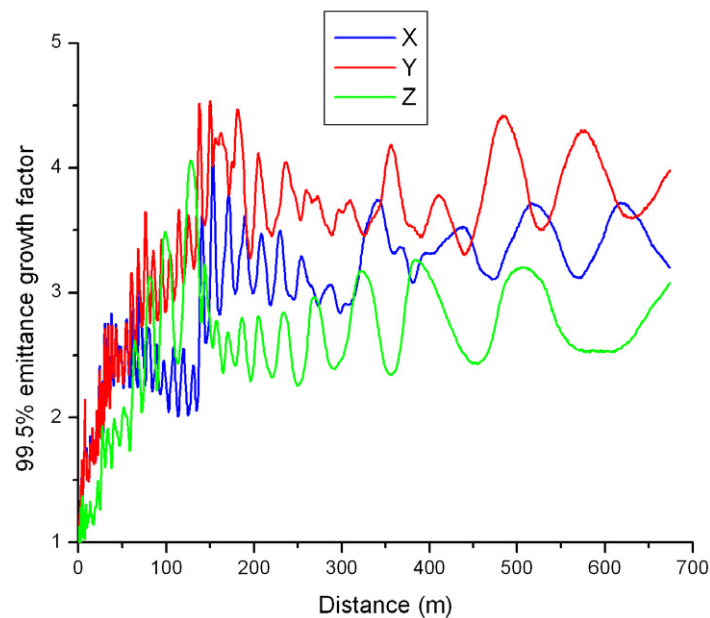


**Figure 25.** 99.5% emittance growth factor along the linac.

MEBT. The final design of the MEBT structure was carried out using a simulation of one million macro-particles to minimize beam losses at the level of  $10^{-6}$ . The following data representing beam losses is normalized to the total current of accelerated particles. Figure 29 shows the losses in the MEBT and in the first several meters of the RT section of the linac. Energy distribution of the lost particles is shown in figure 30. The simulations show that eight particles out of one million are lost with energies above 1.4 MeV as is seen from figure 30. These eight particles become unstable due to longitudinal space charge effects. For the 32 mA beam simulated in the lattice with the same tune, there are three lost particles with energies above 1.4 MeV.

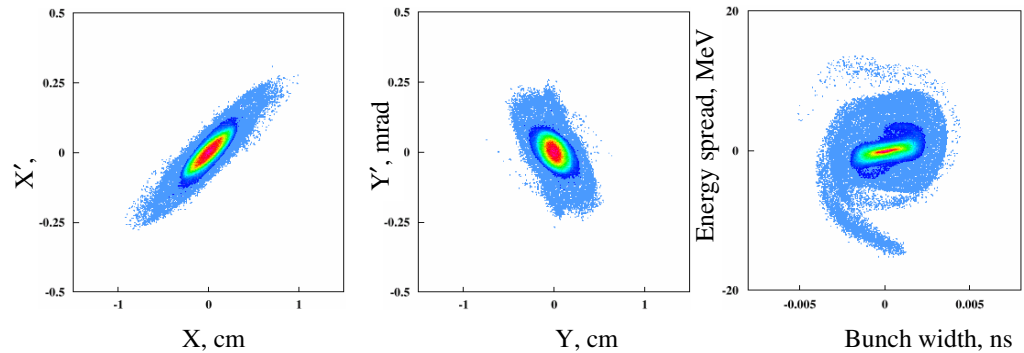


**Figure 26.** Phase space plots of 43.25 mA beam at the end of PD.

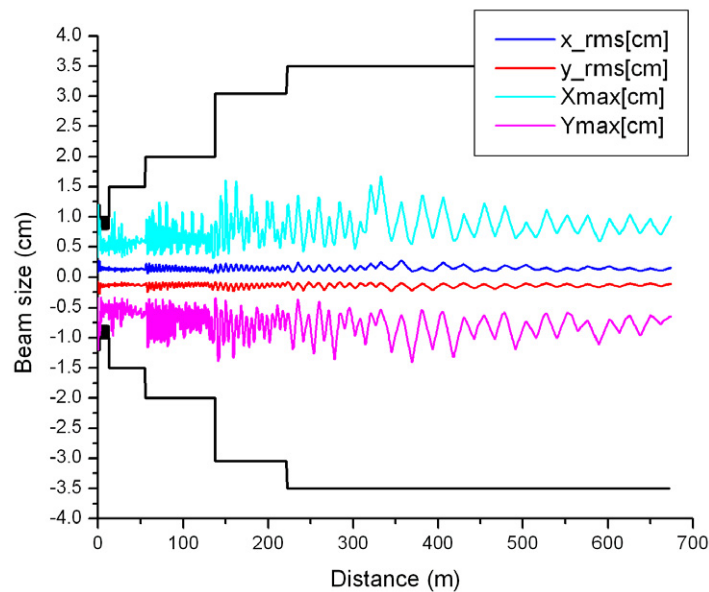


**Figure 27.** Transverse envelopes of 32 mA beam along the linac. The black solid line shows the aperture.

The main driving source of the losses is the distance between two bunchers in the MEBT which results in beam halo development in the longitudinal phase space. The reduction of this distance can eliminate the loss of particles with energies above 2.5 MeV. However, the relative level of the losses is negligible and can be fully accepted in this particular linac.

More detailed information about beam losses will be obtained as a result of beam dynamics simulations including all sources of machine errors following the technique proposed in [24]. To avoid beam losses in a high power linac, it is usually recommended that the ratio of the aperture radius to the beam rms radius should exceed 10 in high energy sections of the linac [42]. As is seen from figure 21, in the PD linac this ratio is above 12 starting from the TSR section.

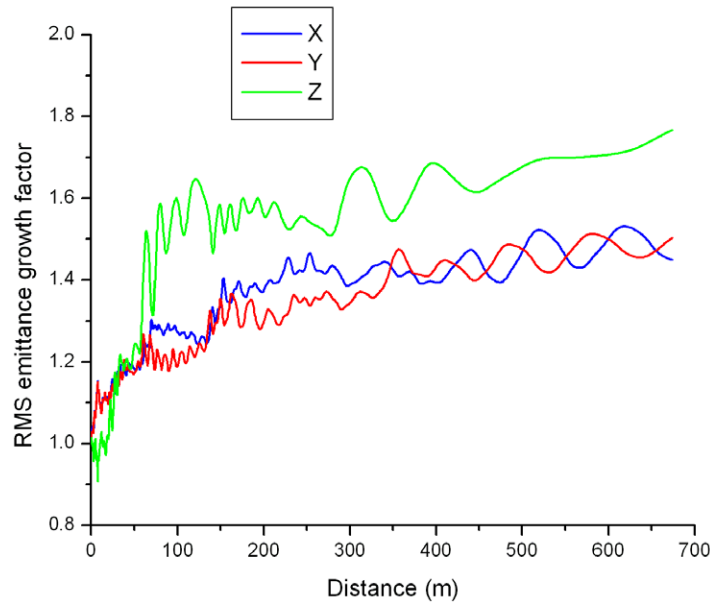


**Figure 28.** RMS emittance growth factor along the linac for 32 mA beam.

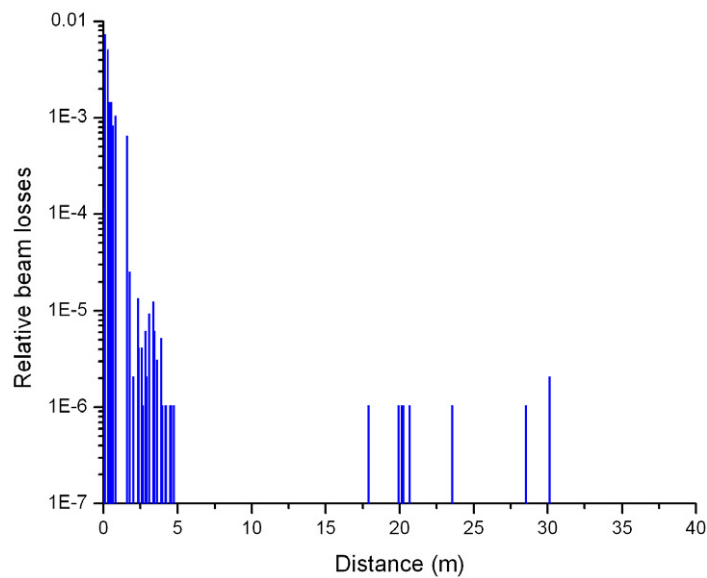


**Figure 29.** Beam losses along the MEBT and in the beginning of the linac. The first 2.5 m represent the MEBT.

## 8. Conclusion

1300 MHz ILC-type SC cavities provide an accelerating voltage of 7.6 GV in the proposed 8 GeV linac. The acceleration from ion source to 420 MeV will be provided by short normal conducting CH cavities followed by spoke-loaded SC cavities operating at the 4th sub-harmonic of the ILC frequency. Utilization of normal conducting cavities up to  $\sim 10$  MeV reduces the number of different types of SC cavities and provides high-quality beam matching in the front

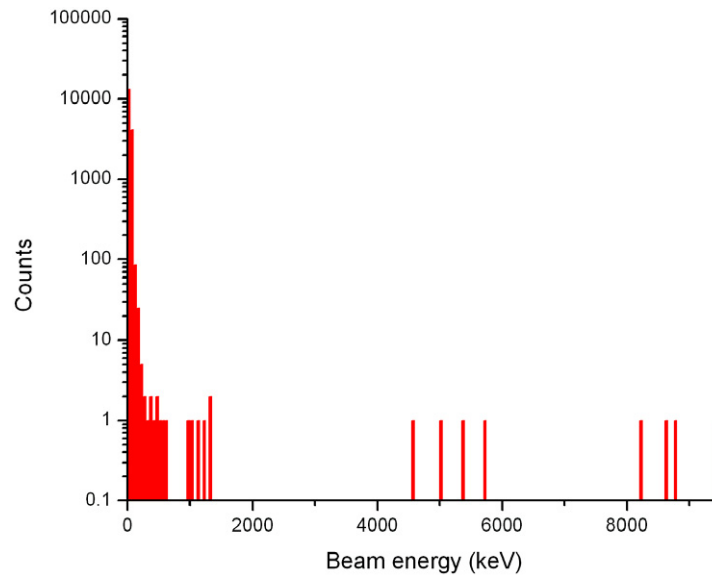


**Figure 30.** Energy spectrum of the lost particles.

end. Focusing by SC solenoids results to a compact lattice below 110 MeV and facilitates the use of high accelerating gradients offered by SSRs. Relatively high beam energy of 420 MeV at the frequency transition 1:4 facilitates beam quality preservation in the high energy section of the linac.

The proposed design of the 8 GeV PD shows that the linac can provide high-quality beams both for the injection into the MI and experiments.

## Acknowledgments

This work was supported by the US Department of Energy, Office of Nuclear Physics, under Contract No. W-31-109-ENG-38. I thank Drs G Appolinari, V N Aseev, G W Foster; I V Gonin, A A Kolomiets, G Lanfranco, A Moretti, B Mustapha, T Nicol, J Nolen, T Page, L Ristori, G V Romanov, C Schmidt, K W Shepard, I Terechkine and R C Webber for helpful discussions and information.

## References

- [1] Foster G W and MacLachlan J A 2002 A multi-mission 8 GeV injector linac as a fermilab booster replacement *Proc. LINAC-2002 (Gyeongju, Korea)* (ed In Soo Ko) p 826
- [2] Foster G W 2005 An 8 GeV Superconducting injector linac paper MOPB001 *Proc. PAC-2005 (Knoxville, TN)* (ed C Horak)
- [3] 2001 *TESLA Technical Design Report DESY 2001-11*
- [4] Holtkamp N 2004 Status of the SNS Linac: an Overview *Proc. LINAC-2004 (Lubeck, Germany)* p 837
- [5] Chou W *et al* 2005 8 GeV  $H^-$  ions: transport and injection *Proc. PAC-2005 (Knoxville, TN)* (ed C Horak) p 1222
- [6] Murin B P *et al* 1978 Ion linear accelerators vol 1 *Problems and Theory* (Moscow: Atomizdat)

- [7] Aune B *et al* 2000 Superconducting TESLA cavities *Phys. Rev. ST. Accel. Beams* **3** 092001
- [8] Shepard K W *et al* 2003 Superconducting intermediate-velocity cavity development for RIA *Proc. PAC-2003 (Portland, OR)* (ed J Chew) [p 1297](#)  
 Delayen J R 2004 Intermediate-velocity superconducting accelerating structures *Proc. LINAC-2004 (Lubeck, Germany)* [p 589](#)
- [9] Kapchinskiy I M 1985 *Theory of Resonance Linear Accelerators (Accelerators and Storage Rings Series)* (New York: Harwood Academic)
- [10] Kato T and Yamazaki Y 1998 Design of the 200 MeV proton Linac for the Japan hadron facility *Proc. LINAC-1998 (Chicago, IL)* (ed C E Eyberger, R C Pardo and M M White) [p 409](#)
- [11] Shepard K W, Ostroumov P N and Delayen J R 2003 High-energy ion linacs based on superconducting spoke cavities *Phys. Rev. ST Accel. Beams* **6** 080101
- [12] Ostroumov P N, Shepard K W and Foster W G 2003 Superconducting linacs for production of multi GeV H<sup>-</sup> or proton beams 2003 *Argonne Physics Division Annual Report* [p 143](#)
- [13] Ostroumov P N, Aseev V N and Kolomiets A A 2006 Application of a new procedure for design of 325 MHz RFQ *J. Instrum. JINST* **1** P04002
- [14] Kang Y 2000 Fast RF ferrite phase shifter for high-power applications *Proc. LINAC-2000 (Monterey, CA)* (ed A W Chao) [p 1012](#)
- [15] Terechkin I *et al* 2005 High power phase shifter *Proc. PAC-2005 (Knoxville, TN)* (ed C Horak) [p 3123](#)
- [16] Bauer P C, Foster G M and Huning M 2004 Simulation of RF control of a superconducting linac for relativistic particles *Proc. EPAC-2004 (Lucerne, Switzerland)* (ed J Chin *et al*) [p 2774](#)
- [17] Tajima T *et al* 2003 Results of two  $\beta=0.175$ , 350-MHz, 2-gap spoke cavities *Proc. PAC-2003 (Portland, OR)* (ed J Chew) [p 1341](#)
- [18] Ostroumov P N *et al* 2005 Front end design of a multi-GeV H-minus Linac *Proc. PAC-2005 (Knoxville, TN)* (ed C Horak) [p 3286](#)
- [19] Li Z *et al* 2004 Design of the R.T. CH-cavity and perspectives for a new GSI proton linac *Proc. LINAC-2004 (Lubeck, Germany)* [p 81](#)
- [20] Romanov G V *et al* 2006 Development of room temperature cross-bar cavities for FNAL proton driver *Abstract presented to LINAC-2006 (Knoxville, TN)*
- [21] Ratti A *et al* 1998 Conceptual design of the SNS RFQ *Proc. LINAC-1998* (ed C E Eyberger, R C Pardo and M M White) [p 276](#)
- [22] Ueno A 2000 RF-test of a 324-MHz, 3-MeV, H<sup>-</sup> RFQ stabilized with PISLs *Proc. Int. Conf. LINAC-2000 (Monterey, CA)* (ed A W Chao) [p 545](#)
- [23] Kolomiets A A 2005 The code DESRFQ, ITEP/ANL *Technical Note*
- [24] Ostroumov P N, Aseev V N and Mustapha B 2004 Beam loss studies in high-intensity heavy-ion linacs *Phys. Rev. ST. Accel. Beams* **7** 090101  
 Aseev V N, Ostroumov P N, Lessner E S and Mustapha B 2005 TRACK: The new beam dynamics code *Proc. PAC-2005 (Knoxville, TN)* (ed C Horak) [p 2053](#)
- [25] Crandall K R *et al* 1998 RFQ Design Codes *Los Alamos National Laboratory Report LA-UR-96* p 1836
- [26] Reiser M 1994 *Theory and Design of Charged Particle Beams* (New York: Wiley)
- [27] [CST Electromagnetic Studio User Manual Version 2.0 January 2004 CST GmbH Darmstadt Germany](#)
- [28] Crandall K R 1994 Ending RFQ vane tips with quadrupole symmetry *Proc. LINAC-1994 (Tsukuba, Japan)* [p 227](#)
- [29] Caspers F 2004 Review of fast beam chopping *Proc. LINAC-2004 (Lubeck, Germany)* [p 578](#)
- [30] Kurennoy S S and Power J F 2000 Meander-line current structure development for SNS fast chopper *Proc. LINAC-2000 (Monterey, CA)* (ed A W Chao) [p 932](#)
- [31] Oshatz D *et al* 2001 Mechanical design of the SNS MEBT *Proc. PAC-2001 (Chicago, IL)* (ed P Lucas and S Webber) [p 1574](#)
- [32] Nath S *et al* 1997 Beam dynamics aspects for the APT integrated linac *Proc. PAC-1997 (Vancouver, Canada)* (ed M Comyn, M K Craddock, M Reiser and J Thomson) [p 1162](#)

- [33] Hofmann I *et al* 2001 *Phys. Rev. Lett.* **86** 2313
- [34] Lawrence G P and Wangler T P 1997 Integrated normal-conducting/superconducting high power proton linac for APT project *Proc. PAC-1997 (Vancouver, Canada)* (ed M Comyn, M K Craddock, M Reiser and J Thomson) [p 1158](#)
- [35] Garnett R *et al* 2001 Conceptual design of a low-beta SC proton linac *Proc. PAC-2001* (ed P Lucas and S Webber) [p 3293](#)
- [36] Ostroumov P N 2002 Design features of high-intensity medium-energy superconducting heavy-ion linac *Proc. LINAC-2002 (Gyeongju, Korea)* (ed In Soo Koo) [p 64](#)
- [37] Fateev A P and Ostroumov P N 1984 Drift spaces effect on longitudinal motion in an ion linac *Nucl. Instrum. Methods* **222** 420
- [38] Senichev Yu and Vasyukhin N 2005 Slot-finger superconducting structure with RF focusing *Phys. Rev. ST. Accel. Beams* **8** 070101
- [39] Stovall J *et al* 2001 Expected beam performance of the SNS linac *Proc. PAC-2001 (Chicago, IL)* (ed P Lucas and S Webber) [p 446](#)
- [40] Gerigk F *et al* 2005 Progress in the design of the SPL normal conducting front-end (<180 MeV) [34th ICFA Advanced Beam Dynamics Workshop HPSL \(Naperville, IL\)](#)
- [41] Crandall K R 1987 TRACE 3-D Documentation *Report LA-11054-MS* Los Alamos
- [42] Jameson R A 1993 On scaling & optimization of high-intensity, low-beam-loss RF linacs for neutron source drivers *AIP Conf. Proc.* **279** 969